

Planar velocity & concentration measurements in a magnetic micromixer with interface front detection

F. Gökhan Ergin¹, Bo Beltoft Watz¹, Kaspars Erglis², Andrejs Cebers²

¹Dantec Dynamics A/S, Skovlunde, Denmark
Gokhan.Ergin@dantecdynamics.com

²University of Latvia, Riga, Latvia

ABSTRACT

Mixing is often a challenge in small scales and substantial research effort is focused on designing high performance micromixers. Active micromixers use various forces to enhance mixing efficiency. Among these, magnetic forces are often preferred as they are non-contact and do not require manufacturing of small moving parts in the microchannel. Laser-based diagnostic tools have great potential in providing multi-parameter information in microfluidics research on mixing. In this work, we extract velocity, concentration and interface front information from a single image pair from a magnetic micromixer undergoing labyrinthine (fingering) instability. The experiments were performed using a MicroPIV system with stroboscopic LED illumination. Velocity information from particle displacements are computed using Least Squares Matching (LSM) and compared with previously published results using Adaptive Cross Correlation (ACC). It turns out that LSM is less sensitive to image contrast; and able to extract most of the useful velocity information from the raw images compared to the processed images. This makes LSM an important global tool for PIV analysis where image pre-processing can be avoided completely, for example in industrial mixing applications. The use of image processing functions proves to be essential in multi-parameter microfluidics: Concentration measurements are performed using absorption imaging after removal of particles using a series of low-pass filters. Results for interface front detection using various other image processing functions are also presented.

Keywords: MicroPIV, magnetic micromixer, image processing, labyrinthine (fingering) instability, local contrast normalization (LCN), difference of Gaussian (DoG) filter, absorption imaging, front detection.

INTRODUCTION

Mixing has a central role in microfluidic processes, and therefore micromixers have substantial focus in microfluidics research. Passive micromixers rely entirely on the fluid pumping energy to induce mixing that is often a result of molecular diffusion between the species. Active micromixers exploit other forms of energy in addition to the fluid pumping energy: pressure fields, sound waves, temperature gradients and magneto-hydrodynamic forces. Because of this, active micromixers provide a better mixing efficiency (shorter mixing length) at the cost of additional components / systems to provide the additional energy for active mixing. The reader is referred to three recent extensive reviews for further details on micromixer technology [1-3].

Among active micromixer alternatives, the magnetic micromixers are often preferred because the mixing energy can be delivered in a non-contact fashion, and the manufacturing of costly micro-scale components is not required. In addition to this, the direction and the magnitude of the magnetic field can be controlled accurately. In the present work, we use magneto-hydrodynamic forces to mix a magnetic and a non-magnetic fluid brought into contact in a Hele-Shaw cell. When a vertical magnetic field is applied, the two fluids try to penetrate into each other in the horizontal plane. Under certain conditions, a finger-like hydrodynamic instability of the interface is observed, often referred to as the labyrinthine instability. The magneto-hydrodynamic labyrinthine (MHDL) instability is analogous to the Rayleigh-Taylor instability of a horizontal surface, where a denser fluid is placed on top of a lighter fluid. The MHDL instability has been the focus of many several theoretical and experimental studies [4-7], but the application of quantitative image-based diagnostics to this instability is relatively recent [8-9].

Many image-based measurement techniques can be applied in microfluidics. Since mixing problems involve the interaction of a flow field and a concentration field of at least 2 different species, simultaneous measurement of velocity and concentration is useful in order to understand the effect of magneto-hydrodynamic manipulation on mixing efficiency. Simultaneous measurements often require multiple-camera detector systems with the same field of view

(FOV). In such systems, the velocity information is detected by one camera and the concentration information by another, where the signal is separated using optical filters. Multiple-camera systems make use of special opto-mechanical sub-assemblies for image combination. Image-combination optics often require careful alignment to produce a similar FOV on both detectors. Since the alignment is never perfect an image calibration is often required before measurements. As an alternative to multiple-detector measurement system, in this experimental study we use a single-camera detector system where velocity, concentration and flame front information is recorded simultaneously on the same image pair. We use Micro Particle Image Velocimetry (μ PIV) for velocity measurements; absorption imaging for concentration measurements; and several image-processing functions for interface front detection.

Micro Particle Image Velocimetry (μ PIV)

PIV technique [10-13] was first applied in planar (2D) flows and provided 2-components (2C) of the velocity field in the measurement plane. In the beginning, the name PIV is often used (and was sufficient) to describe 2D2C PIV; and therefore short three-letter abbreviation was often cited in literature instead of the longer version. In time, several other variations for PIV has been reported in the literature; Digital-PIV, Micro-PIV, Nano-PIV, Holo-PIV, Stereo-PIV, and Tomo-PIV. In this paper, we treat μ PIV as the general name given to a velocimetry technique where calculations are based on particle displacements between two images separated by a short time difference. We make further distinctions on the individual sub-technique using the dimension of the measurement domain (2D vs. 3D) and the number of components measured in this domain (2C vs. 3C). Following this argument, we treat μ PIV as a general name, although it was first used for 2D2C experiments [14-17]: μ PIV is an extension of Particle Image Velocimetry (PIV) technique into mm- or sub-mm sized channels, where velocity measurements can be obtained with μ m resolution. Following the evolution of PIV technique several variations of μ PIV has surfaced: 2D2C Long-range μ PIV [18], 2D3C Stereoscopic μ PIV [19-21], and 3D3C Tomographic μ PIV [22]. In this paper, we restrict our discussions to 2D2C velocity field measurements using μ PIV.

Conventional PIV algorithms often employ the cross-correlation function to identify average particle displacement in an interrogation area. The quality of correlation peak has a strong dependence on the signal-to-noise ratio (SNR), e.g. on the contrast of the particle images. In fact, variable-contrast particle images are not uncommon, especially in two-phase flow applications, for example in mixing studies (Figure 3a). Two image pre-processing techniques δ local contrast normalization (LCN) [23] and Difference of Gaussian (DoG) filter δ have been reported [8,9] to improve the image contrast (Figure 3b). When conventional adaptive cross-correlation (ACC) algorithms are applied on poor contrast images the velocity information in the low-contrast regions is lost (Figure 4a). The image pre-processing scheme described in Reference 8 helps the ACC in recovering the velocity information in the poor contrast regions (Figure 4b). Least Squares Matching (LSM) [24-27, 30-35] is an image matching technique that is less affected by image contrast and therefore more promising in PIV analysis without image pre-processing.

Adaptive Cross-Correlation

Most PIV algorithms in the literature use the cross-correlation function to calculate the average displacement in an interrogation area (IA). The calculation is often performed in the wavenumber domain using FFT in order to speed up the calculation [28]. One limitation of cross-correlation is the trade-off between spatial resolution and dynamic range. Because of this limitation, iterative and adaptive window sizing, window shifting and window deforming techniques are developed to provide high spatial resolution, good accuracy and dynamic range at the same time. After a pixel-accurate calculation of the correlation peak, various fitting functions are used to estimate the peak location with subpixel accuracy. Typical accuracy that can be obtained by digital PIV seems to be around 0.1 pixels, which is limited by the optical resolution of the imaging optics, in other words the smallest possible diffraction spot that the imaging lens can produce [29].

The adaptive cross-correlation (ACC) algorithm used in data processing is implemented in Dynamic Studio v3.40, the commercial PIV package of Dantec Dynamics. Briefly, the implementation is an adaptive and iterative procedure: First, the displacement is calculated on an initial IA, which is larger in size compared to the final IA. Then the initial IA divided into smaller IAs, which are shifted by the displacement calculated in the previous step and deformed according to the velocity gradients in the image. Several passes can be made within each refinement step to further shift & deform the windows to minimize the in-plane particle dropout. The window deformation is performed by adapting the IA shape to velocity gradients. For each IA size, this procedure is repeated until a convergence limit in pixels or a maximum number of iterations is reached. Then a 9-point Gaussian fit is performed on the correlation peak to obtain the displacement field with subpixel accuracy in each pass. A number of FFT window (Hanning, Hamming etc.) and filter functions can be applied during the analysis. Finally, spurious vectors are identified and replaced with a number of validation schemes including peak height, peak height ratio, SNR & Universal Outlier Detection (UOD) [36].

Least Squares Matching

LSM is regaining focus in velocimetry using image-based data. It was already applied in 1994 for volumetric Laser Induced Fluorescence (LIF) [30], in 1996 for tracking 2D particle ensembles [27] and was compared to several correlation-based PIV evaluation algorithms in 2000 [31]. LSM is an optimization procedure that aims at minimizing gray level difference between two successive IA in time. The iterations include translation, rotation, scale and shearing of the IA (Figure 1). In this respect LSM is similar to ACC with window deformation techniques. The main principle of LSM is the application of an affine transformation between two IAs. In addition to the zero-order translational velocity components, the affine transformation takes first order deformations into account during computations. The affine transformation is calculated in an iterative manner (least squares matching) until a minimum in gray value difference between two time steps is reached. The implemented algorithm is described in detail in Reference 33 and the extraction of the velocity gradient matrix is described in Reference 34. In these articles, it is also shown that the assumption of an affine transformation is applicable for small deformations.



Figure 1 Translation, rotation, scale and shearing motions of a fluid element

In the past, LSM received less attention compared to ACC because of longer computation times. A longer computation effort is required due to LSM's iterative nature, and because techniques like FFT cannot be used to speed up the computations [31]. Eventually, the availability of high performance computers and the inclusion of CC as an initial step to LSM have rendered this limitation to an acceptable level [35]. Processing times are nowadays comparable to that of CC based multi-grid, multi-pass algorithms with deforming windows. This makes LSM, once again, an attractive alternative for the measurement of Eulerian velocity fields. The advantages of LSM are reported earlier in References 31 and 32. One main advantage is that LSM can be applied both to (discrete) particle images and to (continuous) scalar images [31,32]. Another significant advantage of using LSM is that the first order deformations of the IA are readily available. Unfortunately, this is not the case for ACC, where the vorticity and other derivatives can only be computed from neighbouring velocity vectors in post-processing. Such a process usually amplifies the noise that can be present in the data.

EXPERIMENTS

The experiments are performed at University of Latvia using a μ PIV system manufactured by Dantec Dynamics (Figure 2a). The system consists of a HiPerformance inverted fluorescence microscope, HiSense MkII 70%-quantum efficiency, double-frame CCD camera with 12-bit image resolution, MicroStrobe pulsed LED illumination device; system controller and advanced synchronization unit with 12.5 ns time resolution. The system controller is equipped with a Dual Xeon 2.33 GHz Quad core processor, 4GB RAM running Windows XP operating system and Dynamic Studio v3.40 software platform for dedicated synchronization, hardware control, database management, image processing library and PIV analyses.

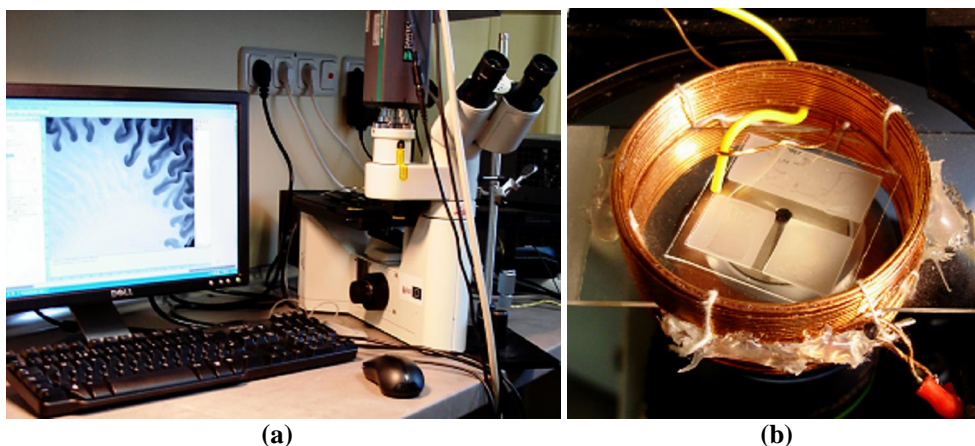


Figure 2 (a) Dantec Dynamics MicroPIV System (b) the Hele-Shaw cell placed in the center of the electromagnet

The Hele-Shaw cell was prepared using two cover glasses separated with 127- μ m-thick *Parafilm*. The channels for fluids and air was cut in *Parafilm* and cured by heating after assembly. The pure solvent is prepared by mixing 100 μ l of

fluorescent particles (2% solid) in 10 ml of distilled water. The colloidal solution of magnetic nanoparticles is prepared by adding fluorescent micro-particles in the magnetic fluid. The water based magnetic fluid was produced from $\text{-Fe}_2\text{O}_3$ magnetic particles with a nominal size of 10 nm. This is achieved by precipitating anionic magnetite from aqueous solution of Fe^{2+} and Fe^{3+} chlorides using ammonium hydroxide. A few drops of magnetic fluid were introduced on the right side of cell using a micropipette, until the capillary forces filled one half of the cell with magnetic fluid. Then, few drops of pure solvent were introduced from the other side until the pure solvent came in contact with the magnetic fluid. The fluorescent seeding particles are carboxylate-modified microspheres with 1 μm diameter. The particles are Nile-red fluorescent (between 535-575 nm) and are quite suitable for high-resolution MicroPIV applications. The particles are introduced both in the magnetic fluid and in the solvent as light scatterers. The Hele-Shaw cell was placed in the center of an electro-magnet, a 38-turn-coil of 0.7-mm-diameter wire (Figure 2b). A current of 2A from *Keeco* BOP 20-10M power supply produced a magnetic field strength of 1.8 mT in the central part of the coil. The field was applied before pure solvent mixed with magnetic fluid.

The second frame of the raw image pair acquired with this setup is shown in Figure 3a. The pixel value distribution of an image depends on the scattering mode used in the acquisition: Side-scatter reflection (or refraction for transparent seeding) will often result in an image with bright particles on a dark background. Alternatively, forward-scatter illumination, often used in shadow imaging and transmission microscopy applications will result in images with dark particles (shadows) on a bright background. Because transmission illumination is used during the experiment, the particle shadows are imaged on the CCD detector.

Two image pre-processing techniques δ local contrast normalization (LCN) [23] and Difference of Gaussian (DoG) filter [23,8] δ are known to improve the image contrast (Figure 3b). In this image, the field of view (FOV) is 867 μm x 660 μm using a 10x objective and a 1x C-mount adapter (1550 pix/mm). The trigger rate is set to 3 Hz; time between pulses is 81,68 ms, first and second pulse duration is 450 μs , and 550 μs respectively. The dark region is the colloidal solution of magnetic nano-particles and fluorescent particles. The bright region is the pure solvent containing 1- μm -diameter fluorescent particles, which are visible as shadows. The image pair is acquired several seconds after the colloidal solution and solvent are brought in contact.

RESULTS

Velocity (u, v) & Vorticity (w_z) measurements

Because the intention is to make a comparison between ACC and LSM, the velocity and the vorticity results are positioned on one page in a matrix format (Figure 3, 4 and 5), with the same display settings. Figure 3 includes the raw particle image on the left, and the processed particle image [8] on the right. In the following 2 figures, the same analysis is applied on the raw and processed images within the same figure (ACC in Figure 4 and LSM in Figure 5) and the results are positioned under the particle images they originate from (results originate from raw images on the left and from processed images on the right).

The vector field in Figure 4 is obtained using an ACC algorithm that is different than what was reported in Reference 8: Since the mean displacement is small in the entire image (~ 5 pixels) and fairly homogenous we use a 50% overlapped, 32-pixel-wide square IA with no window refinement steps. A phase-only Gaussian filter is used in order to make the correlation more tolerant to variations in the background. Spurious vectors are identified and replaced (red vectors Figure 4) using a peak height ratio validation scheme (1.2) in combination with a UOD [36] in a 3x3 neighborhood with a detection threshold of 2.0 and a normalization level of 0.1 pixels. The convergence limit for deforming windows was 0.01 pixels or a maximum 100 iterations. No further FFT windowing or local smoothing is applied during the analysis. Every second vector is displayed in both directions. The corresponding vorticity map is also displayed with warm colors indicating positive, cold colors indicating negative and the green color indicating zero vorticity.

The vector fields obtained in Figure 5 use the LSM algorithm with 31-pixel-wide square IA δ . Because the iterative rotation motion is applied around the center pixel of each IA, LSM requires an odd number of pixels in the IA dimension. This makes comparison of LSM and ACC vector maps somewhat complicated, as vector positions are always shifted. Vector comparisons are only possible by re-sampling the vector field obtained by one method (either ACC or LSM) on the vector field positions of the other method. In order to keep a similar vector density, IA centers are spaced every 16 pixels corresponding to a 50% overlap in ACC. As LSM is an iterative technique, a convergence criterion has to be defined during processing: here we use a convergence level of 0.01 on the sum-squared gray value residual [33]. In case of no convergence a maximum number of 10^4 iterations were performed. In order to save computation time, the input for initial displacement was calculated using a basic cross correlation scheme. Once again, no further local smoothing is applied and every second vector is displayed in both directions. Spurious vectors are replaced using the same UOD scheme and settings as in the case of ACC (red vectors in Figure 5). The corresponding vorticity map is overlaid with the display settings as in the case of ACC.

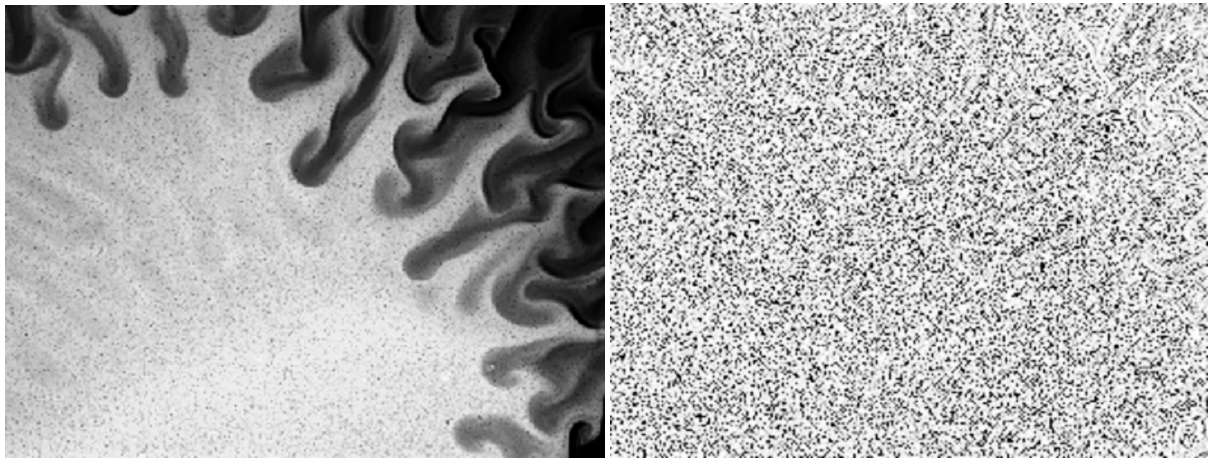


Figure 3 (a) Particle image of the magnetic mixing experiment, displaying the labyrinthine instability between the magnetic fluid (dark) and solvent (bright region). (b) Processed image after LCN and DoG filter. [From Reference 8]

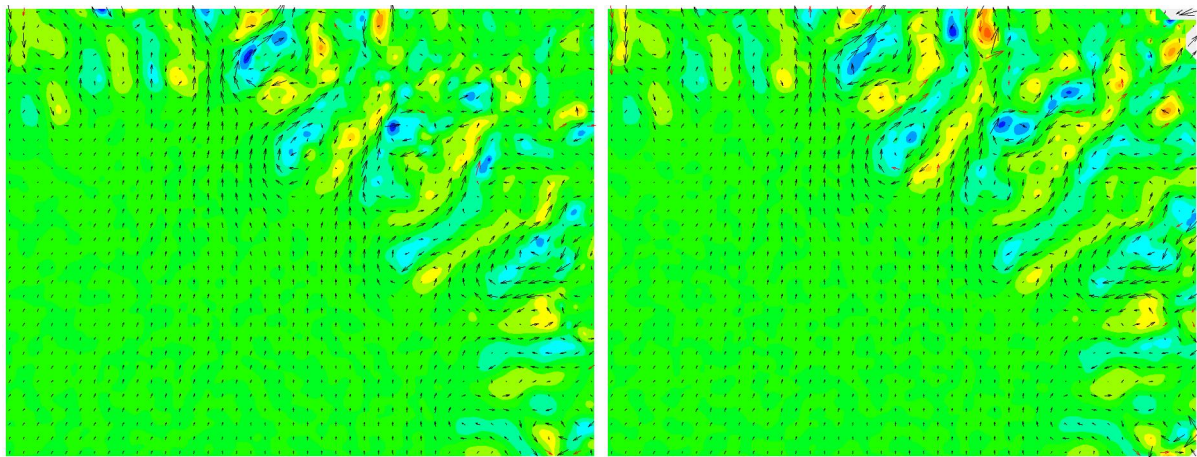


Figure 4 Adaptive cross correlation applied on (a) raw images, (b) processed images. Every second vector is displayed, replaced spurious vectors shown in red. Colors indicate vorticity; legend is shown under Figure 5.

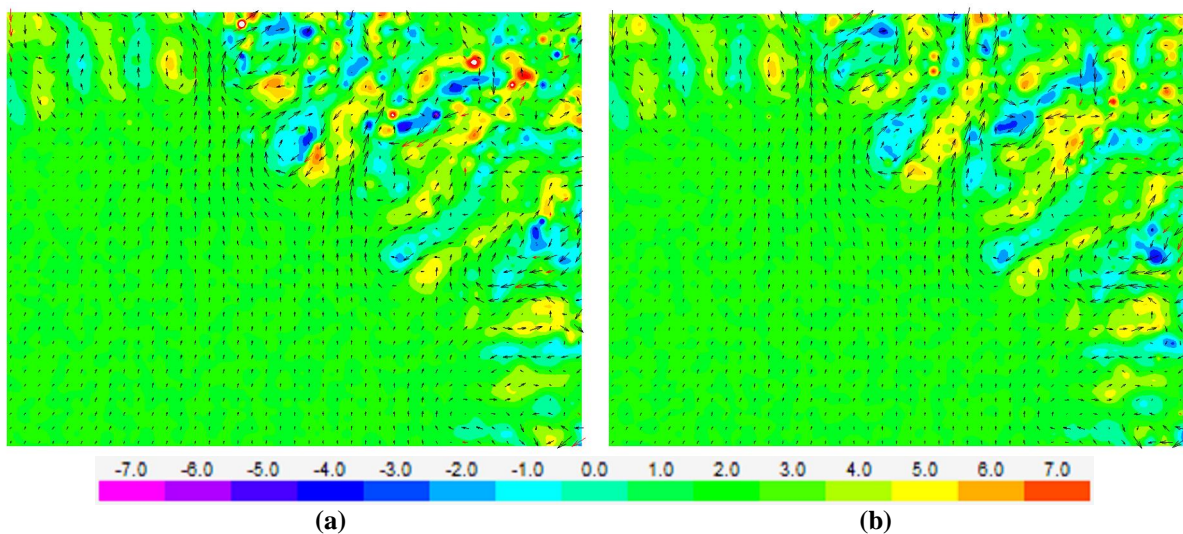


Figure 5 LSM applied on (a) raw images, (b) processed images. Every second vector is displayed, replaced spurious vectors shown in red. Iteration convergence limit is 0.01, and colors indicate vorticity.

A number of qualitative observations can be made on Figures 4 and 5: (i) Very few spurious vectors were identified by both techniques, and this establishes confidence on the presented results. (ii) It is apparent that without prior image processing, conventional ACC algorithms fail to detect the flow field in the darker regions where the image contrast is poor (top right corner of Figure 4a vs. Figure 4b). (iii) LSM algorithm is able to extract a lot more correct velocity information from the raw images compared to ACC (Figure 4a vs. Figure 5a). (iv) ACC vorticity maps are smoother, and the values are slightly less than those for LSM. This can be explained by the following: the vorticity calculation is performed after the velocity vector calculation in the case of ACC; whereas, the vorticity and other first order spatial derivatives are part of the vector calculation during LSM. It is not certain which calculation is more accurate with the experimental data; synthetic particle images could be used to assess the accuracy of velocity & vorticity calculation.

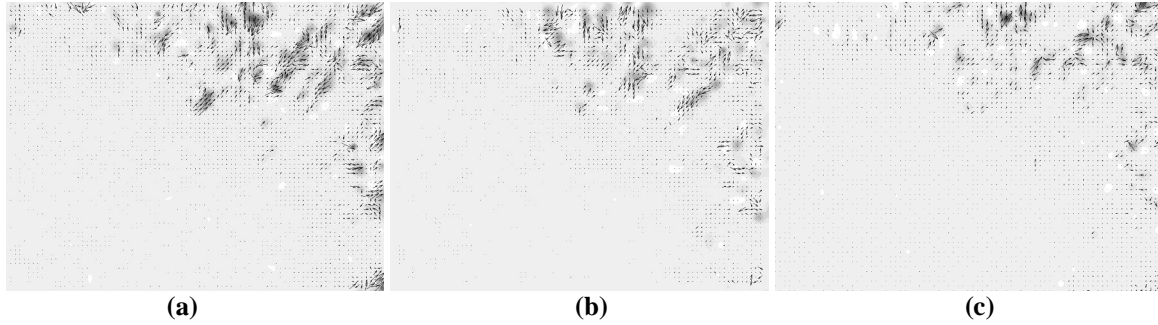


Figure 6 Difference of vector maps: (a) Figure 4a and 4b, (b) Figure 5a and 5b, (c) Figure 4b and 5b. Every vector is displayed, gray levels indicate vector length.

A more quantitative analysis can be made using the difference of vector maps in Figures 4 and 5 (Figure 6), where the scalar gray levels indicate the length of the vectors. First observation is that both methods calculate the same vector field in the water phase, where poor contrast is not a limitation (bottom left regions of Figure 6a, b, and c). Two additional comparisons can be made: the effect of image processing for each method, and the performance of each method applied on the same data. It is clear that both methods benefit from image processing to improve the contrast (Figure 6a and b). Also, ACC is more sensitive to image contrast, since it benefits the more from image pre-processing (Figure 6a) when compared to LSM (Figure 6b). A final observation is that, there is still a small difference between LSM and ACC even when both are applied on processed images (Figure 6c). In this figure, ACC vector map is resampled on the LSM vector positions using a thin-plate spline interpolation. Once again, synthetic particle images could be used to assess the accuracy of velocity calculation in the poor-contrast regions. For the sake of completeness, a subpixel distribution is also calculated for Figure 4b, 5a and 5b to check any possible pixel locking phenomena. For all three cases, (ACC on processed data, LSM on processed data and LSM on raw data) no pixel locking is detected (Figure 7, 8 and 9).

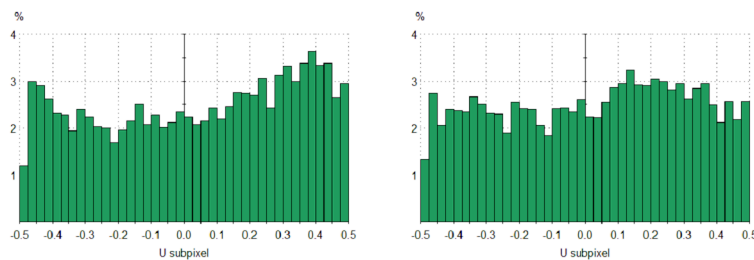


Figure 7 Subpixel distribution of ACC applied on processed images

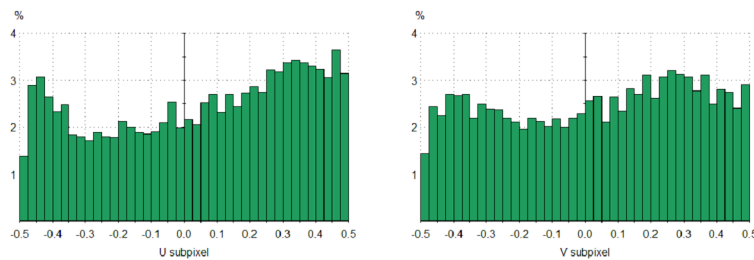


Figure 8 Subpixel distribution of LSM applied on processed images

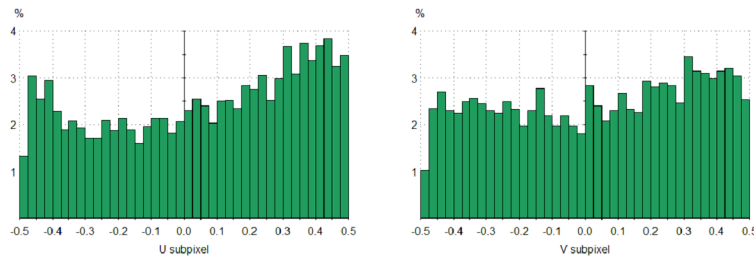


Figure 9 Subpixel distribution of LSM applied on raw images

Concentration measurements

In Reference 8, the purpose was to isolate the particles from the background (Figure 3b) to get a good signal-to-noise ratio (SNR) for velocity measurements. However, the background, i.e. bright and dark regions without particles, contains useful information about the concentration of the two species. Concentration information is quite important for mixing problems in the identification of diffusion lengths etc. If particle images can be separated from the background, it should also be possible to separate the background image information from the particles using image-processing functions: Since the fluorescent seeding particle shadows are recorded with darker gray values, we use a local maximum filter in a 15x15 neighborhood. The resulting gray level distribution is a result of absorption of transmitted light by the magnetic fluid. In fact, the magnetic fluid is a dense emulsion of magnetic nano-particles, which cannot be resolved by the microscope, and appear as a dark cloud. Although Micro Laser Induced Fluorescence (μ LIF) technique would be a better choice to make quantitative concentration measurements; it cannot be applied on the image pair in hand since the magnetic nano-particles are not fluorescent, and the scattering mode is not suitable for LIF. Nevertheless, as a proof-of-concept for multi-parameter measurements, absorption imaging can be used to obtain a rough estimate of the concentration field for this problem. By using the maximum and minimum pixel values in the background image, a region-of-interest (ROI) calibration can be made similar to those in diagnostics of combustion species using LIF: The highest pixel value is observed when the light transmission is at its maximum; i.e. absorption by the magnetic fluid is a minimum. Similarly, the lowest pixel value is observed when the light transmission is at its minimum; i.e. absorption by the magnetic fluid is a maximum. Assuming that the magnetic fluid concentration varies linearly with the light intensity, the entire image can be processed to give an estimate on the concentration field during mixing (Figure 10). In this figure blue color indicates pure water phase whereas the red color indicates the magnetic fluid phase.

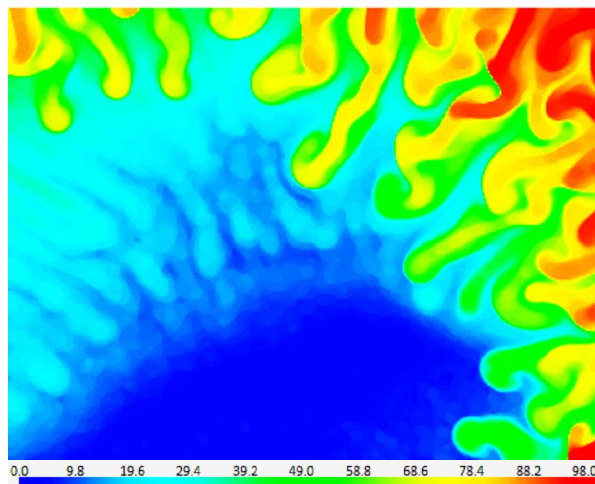


Figure 10 Magnetic fluid concentration field estimated using absorption imaging

Front detection

Experimental identification and tracking of the interface location is another key parameter for verification of theoretical and computational studies, not limited to mixing: The flame front in combustion diagnostics, shock wave in supersonic flows, droplet boundary in droplet-based microfluidics are all examples of sharp gradients. In addition to this, many hydrodynamic instability problems involving two-phase flows, such as Rayleigh-Taylor, Kelvin-Helmholtz and Plateau-Rayleigh instability, are a result of amplified perturbations of the interface. From a PIV perspective, such interface fronts place a well-defined boundary on a sharp velocity gradient, and the interface front information could be used as a dynamic mask in defining two different zones for velocity computation.

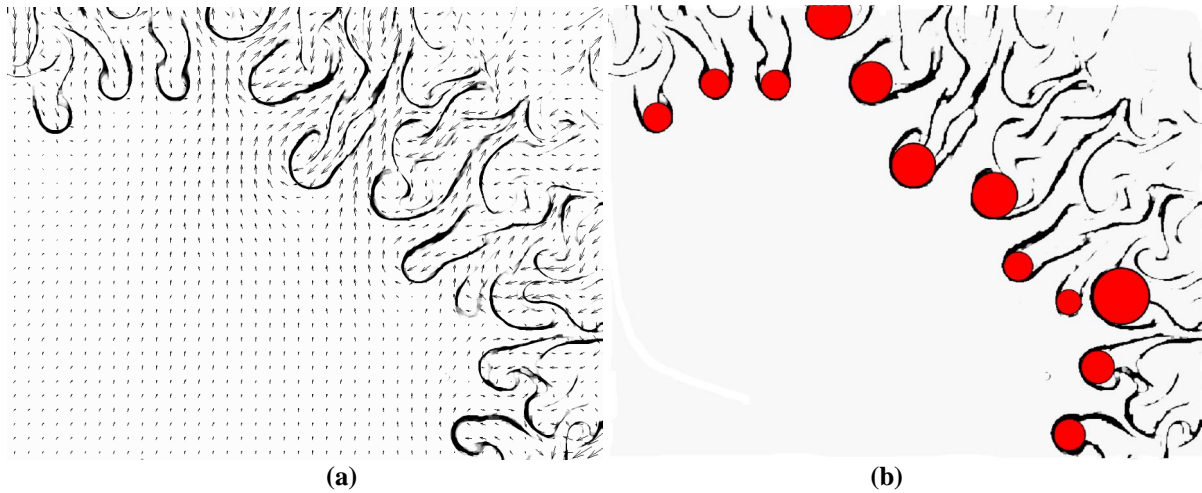


Figure 11 (a) Interface location and (b) mean wavelength measurement for the labyrinthine instability

The MHD instability has been subject to extensive theoretical and experimental research. The first experimental evidence of ‘finger-like’ structures at the interface was provided in Reference 4, with observations on the characteristic spatial period of the pattern. The fingering phenomenon is observed when the magnetic field strength exceeds a threshold value [5], i.e. the magnetic and non-magnetic phases begin to penetrate into each other (Figure 11a). Additionally, ‘long fingers’ are observed under the effect of milder magnetic fields and ‘splitting fingers’ under the effect of stronger magnetic fields [7]. The parametric study reveals that time, cell height and magnetic field strength individually affect the characteristic wavelength of the fingers. The characteristic wavelength was estimated earlier as the mean distance between fingers [7]. In Reference 7, the distance between 10 aligned fingers were measured and averaged to obtain the mean period. In our case and in general, the fingers may not be aligned perfectly (Figure 11a). The interface location (black lines) in this figure is calculated by a series of image processing functions including the Prewitt edge detection filter. The Prewitt operator is a combination of a horizontal and a vertical gradient filter, operating on a 3x3 kernel. This is followed by a number of opening, closing, erosion and threshold filters to isolate the interface. Then, circles with different diameters are fitted manually on the 12-neighboring fingertips visible in the FOV (Figure 11b), and center-to-center distances are measured. Although the method is not yet automated, it provides a rough estimate on the characteristic wavelength. The mean finger-to-finger distance is found as 156 μm and the mean fingertip diameter is found as 85 μm for a magnetic field strength of 1.8mT and a channel thickness of 127 μm . These findings are in agreement with the steady state values reported in Reference 7: (i) approx. 125 μm mean finger period for a magnetic field strength of 2.0mT and cell thickness of 125 μm (Figure 5 in [7]); and (ii) approx. 130 μm mean finger period for a magnetic field strength of 2.0mT and cell thickness of 100 μm (Figure 6 in [7]).

CONCLUSION & FUTURE WORK

It is demonstrated that careful use of image processing functions enables multiple parameter measurements on a single image pair, and retrieve important simultaneous information about the flow field. The performance of two established methods (ACC and LSM) is compared during velocity and vorticity measurements, and both are found to benefit from pre-processing to improve image contrast. Neither method suffers from pixel locking on these images. LSM is found to be less sensitive to image contrast variations. Performance and accuracy of LSM is equivalent to ACC in high-contrast regions of the analyzed image. As a result, LSM can be used as an alternative to ACC in cases where image pre-processing is not possible, or not desired. Concentration field is estimated based on the amount of light absorption and the interface front is calculated using the Prewitt operator in combination with other standard image processing functions. The observed mean finger distance is in agreement with previously reported values. The manual calculation of mean period between fingers and the mean diameter forms the foundation of future work where these calculations can be performed in a more systematic fashion. The current work provides substantial experience in data processing for future work, which includes a similar mixing experiment investigating flow dynamics using time resolved data.

REFERENCES

- [1] Nguyen NT and Wu Z *Micromixers – a review* *J. Micromech. Microeng.* (2005) 15: R1-R16
- [2] Hessel V, Löwe H and Schönfeld F *Micromixers – a review on passive and active mixing principles* *Chemical Engineering Science* 60 (2005) pp.2479-2501
- [3] Capretto L, Cheng W, Hill M, and Zhang X *Micromixing within microfluidic devices* *Top Curr Chem* 304 (2011) pp.27-68
- [4] Maiorov MM and Tsebers AO *Magnetic microconvection on the diffusion front of ferroparticles* *Magnetohydrodynamics* 19 (1983) pp. 376-380
- [5] Cebers A *Stability of diffusion fronts of magnetic particles in porous media (Hele-Shaw cell) under the action of external magnetic field* *Magnetohydrodynamics* 33 (1997) pp. 48-51
- [6] Igonin, M and Cebers A, *Labyrinthine instability of miscible magnetic fluids* *Physics of Fluids* 15 (2003) pp.1734-1744.
- [7] Derec C, Boltenhagen P, Neveu S, and Bacri J-C *Magnetic instability between miscible fluids in a Hele-Shaw cell* *Magnetohydrodynamics* 44 (2008) pp.135-142
- [8] Ergin FG, Watz BB, Erglis K and Cebers A *Poor-contrast particle image processing in micro scale mixing* *Proceedings of the ASME 10th Biennial Conference on Engineering Systems Design and Analysis* (2010) #24900
- [9] Erglis K, Tatulchenkov A, Kitenbergs G, Petrichenko O, Ergin FG, Watz BB, and Cebers A *Magnetic field driven micro-convection in the Hele-Shaw cell* *Journal of Fluid Mechanics* 714 (2013) pp.612-633
- [10] Raffel M, Willert CE, Wereley ST, and Kompenhans J. *Particle Image Velocimetry – A Practical Guide* *Springer-Verlag* (2007)
- [11] Adrian RJ and Westerweel J *Particle Image Velocimetry* *Cambridge University Press* (2010)
- [12] Adrian, RJ *Twenty years of particle image velocimetry*, *Experiments in Fluids* 39 (2005) pp.159-169.
- [13] Willert C *Recounting twenty years of digital PIV, its origins and current trends* *Proceedings of 8th Int. Symposium on Particle Image Velocimetry – PIV09* (2009)
- [14] Santiago JG, Wereley ST, Meinhart CD, Beebe DJ, Adrian RJ *A particle image velocimetry system for microfluidics* *Experiments in Fluids* 25 (1998) pp.316-319.
- [15] Meinhart CD, Wereley ST, Santiago JG *PIV measurements of a microchannel flow* *Experiments in Fluids* 27 (1999) pp.414-419
- [16] Wereley ST and Meinhart CD, *Recent Advances in Micro-Particle Image Velocimetry* *Annu. Rev. Fluid Mech.* 42 (2010) pp.557-576
- [17] Lindken R, Rossi M, Grosse S, and Westerweel J *Micro-Particle Image Velocimetry (μ PIV): Recent developments, applications, and guidelines* *Lab Chip* 9 (2009) pp.2551-2567
- [18] Kähler CJ, Scholz U, and Ortmanns J *Wall-shear-stress and near-wall turbulence measurements up to single pixel resolution by means of long-distance micro-PIV* *Experiments in Fluids* 41 (2006) pp.327-341
- [19] Lindken R, Westerweel J, Wieneke B *Stereoscopic micro particle image velocimetry* *Experiments in Fluids* 41 (2006) pp.161-171
- [20] Brede M, Witte M, Leder A *Stereo-Micro PIV measurements of the three-dimensional separated flow in the wake of a backward facing step* *Proc. 13th Int Symp on Applications of Laser Techniques to Fluid Mechanics* (2006) #1051
- [21] Hagsäter SM, Westergaard CH, Bruus H and Kutter JP *A compact viewing configuration for stereoscopic micro-PIV utilizing mm-sized mirrors* *Experiments in Fluids* 45 (2008) pp.1015-1021
- [22] Kim H, Westerweel J, and Elsinga GE *Comparison of Tomo-PIV and 3D-PTV for microfluidic flows* *Meas. Sci. Technol.* 24 (2013) 024007 (12pp)
- [23] Westerweel J *Digital Particle Image Velocimetry – Theory and Application*, *Delft University Press* (1993)
- [24] Ackermann F *High precision digital image correlation* *Proceedings of the 39th Photogrammetric Week, Schriftenreihe der Universität Stuttgart* 9 (1984) pp.231-243.
- [25] Förstner W *Quality assessment of object location and point transfer using digital image correlation techniques.* *International Archives of Photogrammetry* 25-III A3a (1984) pp.197-217.
- [26] Grün A *Adaptive least squares correlation - a powerful image matching technique* *South African Journal of Photogrammetry, Remote Sensing and Cartography* 14 (1985) pp.175-187.
- [27] Gui L, Merzkirch W *A method of tracking ensembles of particle images* *Exp. Fluids* 21 (1996) pp.465-468

- [28] Willert CE and Gharib M "Digital Particle Image Velocimetry" Experiments in Fluids 10 (1991) pp.181-193
- [29] Westergaard CH, Madsen BB, Marassi M and Tomassini EP "Accuracy of PIV signal in theory and practice" Proc. 5th International Symposium on PIV (2003)
- [30] Maas HG, Stefanidis A, Grün A "From pixels to voxels - tracking volume elements in sequences of 3-d digital images" Int. Arch Photogramm Remote Sens (1994) 30(3/2)
- [31] Gui L and Merzkirch W "A comparative study of the MQD method and several correlation-based PIV evaluation algorithms" Exp. in Fluids 28 (2000): pp.36-44
- [32] Tokumaru PT and Dimotakis PE "Image Correlation Velocimetry" Exp. In Fluids 19 (1995) pp.1-15
- [33] Westfeld P, Maas HG, Pust O, Kitzhofer J and Brücker C "3-D least squares matching for volumetric velocimetry data processing" 16th Int Symp on Applications of Laser Techniques to Fluid Mechanics, Lisbon (2010)
- [34] Kitzhofer J, Westfeld P, Pust O, Maas HG and Brücker C "Estimation of 3D deformation and rotation rate tensor from volumetric particle data via 3D Least squares matching" 16th Int Symp on Applications of Laser Techniques to Fluid Mechanics, Lisbon (2010)
- [35] Kitzhofer J, Ergin FG, Jaunet V "2D Least Squares Matching applied to PIV Challenge data (Part 1)" Proceedings of the 16th Int Symp on Applications of Laser Techniques to Fluid Mechanics (2012)
- [36] Westerweel J and Scarano F "Universal outlier detection for PIV data" Exp. In Fluids 39 (2005): pp.1096-1100